Ultrastructural evidence for self-replication of Alzheimer-associated Aβ42 amyloid along the sides of fibrils

Mattias Törnquist[a,1], Risto Cukalevski[a,2], Ulrich Weininger[b,3], Georg Meisl[c], Tuomas P. J. Knowles[c,d], Thom Leiding[a], Anders Malmendal[a,e,4], Mikael Akke[b], and Sara Linse[a,e,1]

[a]Department of Biochemistry and Structural Biology, Lund University, 221 00 Lund, Sweden; [b]Department of Biophysical Chemistry, Lund University, 221 00 Lund, Sweden; [c]Department of Chemistry, University of Cambridge, CB2 1EW Cambridge, United Kingdom; [d]Cavendish Laboratory, Department of Physics, University of Cambridge, CB3 0HE Cambridge, United Kingdom; and [e]NanoLund, Lund University, 221 00 Lund, Sweden

Edited by F. Ulrich Hartl, Max Planck Institute of Biochemistry, Martinsried, Germany, and approved April 15, 2020 (received for review October 30, 2019)

The nucleation of Alzheimer-associated Aβ peptide monomers can be catalyzed by preexisting Aβ fibrils. This leads to autocatalytic amplification of aggregate mass and underlies self-replication and generation of toxic oligomers associated with several neurodegenerative diseases. However, the nature of the interactions between the monomeric species and the fibrils during this key process, and indeed the ultrastructural localization of the interaction sites have remained elusive. Here we used NMR and optical spectroscopy to identify conditions that enable the capture of transient species during the aggregation and secondary nucleation of the Aβ42 peptide. Cryo-electron microscopy (cryo-EM) images show that new aggregates protrude from the entire length of the progenitor fibril. These protrusions are morphologically distinct from the well-ordered fibrils dominating at the end of the aggregation process. The data provide direct evidence that self-replication through secondary nucleation occurs along the sides of fibrils, which become heavily decorated under the current solution conditions (14 μM Aβ42, 20 mM sodium phosphate, 200 μM EDTA, pH 6.8).

fibril formation | amyloidosis | neurodegeneration | self-assembly | aggregation mechanism

Alzheimer's disease is a devastating neurodegenerative disease with increasing prevalence (1). The exact molecular events leading to onset and spreading of pathology remain to be defined. However, a key molecular process, which has been linked to the pathology is the aggregation of amyloid β-peptides, particularly of peptides corresponding to residues 672 to 711 (Aβ40) or 672 to 713 (Aβ42) of the amyloid precursor protein, into amyloid fibrils via smaller intermediates (2, 3). According to the current consensus in the field, monomers and fibrils are relatively inert, whereas the most neurotoxic species can be found among the smaller aggregates, oligomers (4, 5). The majority of these toxic species seems to be formed in solutions containing both monomeric and fibrillar species (6) through the process of secondary nucleation at the fibril surface both for Aβ40 (7) and Aβ42 (8, 9).

Secondary nucleation is a general microscopic step in processes involving nucleation and growth, observed for example in the crystallization of small molecules (10–12) and the polymerization of sickle-cell hemoglobin (13). Recent simulations have shown that many universal features of secondary nucleation can be described by minimal or coarse-grained models (14, 15). Recent findings confirm that secondary nucleation of Aβ42 is prevalent also in human cerebrospinal fluid (16). The rapid multiplication of aggregate concentration due to secondary nucleation, and the potential connection of this process with toxicity and spreading of amyloid diseases, motivates further studies into the molecular determinants and mechanism of secondary nucleation.

A series of studies of intrinsic and extrinsic factors in Aβ aggregation indicate that secondary nucleation can be accelerated in situations where hydrophobicity is enhanced or electrostatic repulsion between monomers and fibrils is diminished through mutation, pH variation, or salt screening (17–22). Secondary nucleation thus requires the association of monomers to the fibril surface and the process can be completely blocked in the presence of competing surface binders such as the Brichos chaperone (9) or fibril-specific antibodies (23, 24). Under certain conditions, the association of monomers of Aβ40 or Aβ42 with fibrils of the same peptide occurs so fast that the fibril surface becomes saturated and the rate of secondary nucleation becomes independent of the free monomer concentration (7, 18, 25).

Despite being dominated by secondary nucleation, the aggregation process of Aβ seems to typically result in unbranched

Significance

Two unresolved problems in Alzheimer's disease (AD) are its onset and propagation, linked to Aβ peptide aggregation. Fibrils of Aβ42 may grow by monomer addition at their ends. Additionally, through secondary nucleation, fibrils catalyse the formation of new aggregates from monomer on their surface, thereby generating oligomeric species that are toxic to brain tissue. Insights into the structural transitions occurring during secondary nucleation will facilitate the design of therapies to limit the neurotoxicity in AD, but such information is currently lacking. This study identifies conditions that allow the capture of reaction intermediates of secondary nucleation for the purpose of ultrastructural characterization. These reaction intermediates are morphologically distinct from mature fibrils and cover the sides of fibrils during an on-going aggregation reaction.

Author contributions: M.T., R.C., U.W., M.A., and S.L. designed research; M.T., R.C., U.W., G.M., and A.M. performed research; T.L. and S.L. contributed new reagents/analytic tools; M.T., R.C., U.W., G.M., T.P.J.K., A.M., M.A., and S.L. analyzed data; and M.T. and S.L. wrote the paper.

The authors declare no competing interest.

This article is a PNAS Direct Submission.

Data deposition: The complete set of cryo-EM images has been deposited to Figshare (DOI: 10.0.23.196/m9.figshare.4715243.

[1]To whom correspondence may be addressed. Email: sara.linse@biochemistry.lu.se or mattias.tornquist@biochemistry.lu.se.

[2]Present address: Recovery Pilot Plant Development, Novozymes, 2880 Bagsværd, Denmark.

[3]Present address: Biophysics Division, Department of Physics, Institute of Physics/Biophysics, Martin Luther University Halle-Wittenberg, 06120 Halle (Saale), Germany.

[4]Present address: Department of Science and Environment, Roskilde University, DK-4000 Roskilde, Denmark.

This article contains supporting information online at https://www.pnas.org/lookup/suppl/doi:10.1073/pnas.1918481117/-/DCSupplemental.

First published May 21, 2020.

fibrils, as observed in electron microscopy images of mature fibrils (26–30). A few studies have revealed occurrences of new fibrils branching from the surface of existing ones, both in mature fibrils at the end of the reaction (31) and throughout the aggregation time course (32, 33). These branching events may be the result of secondary nucleation, but their scarcity indicates that in the conditions studied the majority of products formed after secondary nucleation detach from their parent fibril fast enough to escape detection.

Among the major unresolved questions regarding secondary nucleation (21), are the location of the catalytic site on the fibril surface, whether these sites are distinct or diffuse, and whether both the ordered part (residues 15 to 42) (34, 35) and the more flexible N terminus (residues 1 to 14) play a role in the process. It is also unclear at what stage in the process the detachment occurs, what the size and structure of the detaching species might be, and whether conversion from prefibrillar oligomeric structure to fibrillar structure occurs prior to, during, or after the detachment.

Here we present kinetic and ultrastructural evidence for the accumulation of reaction intermediates of secondary nucleation along the entire length of fibrils. We took advantage of initial observations that an ongoing Aβ42 aggregation process appears to be temporarily retarded under certain solution conditions, outlined below, which provides an opportunity to capture transient species present during secondary nucleation for detailed structural investigation by cryo-electron microscopy (cryo-EM). We identified suitable conditions for such investigation in terms of the solution pH by monitoring both the depletion of Aβ42 monomer using NMR spectroscopy and the build-up of ordered fibrils using thioflavin T (ThT) fluorescence and static light scattering. Guided by the resulting time-course data, we extracted samples for cryo-EM imaging at specific time points along the reaction. To investigate the link between the observed structures and secondary nucleation, we performed experiments in the presence of a known inhibitor of secondary nucleation, the Brichos chaperone domain. We further took advantage of the high specificity of secondary nucleation that prevents Aβ42 and Aβ40 to cross-seed each other in this process and studied samples where premade seeds of Aβ42 or Aβ40 were added to monomers of either peptide. Taken together, the results reveal a reaction intermediate, morphologically distinct from mature fibrils, building up along the entire length of fibrils, but only under conditions where secondary nucleation is a prominent process.

Results

NMR Spectroscopy. We used NMR spectroscopy to monitor the free monomer concentration in solution during the aggregation process for Aβ42 at pH values ranging from 6.2 to 8.6 (Fig. 1*A*). Signals from fibrils and large oligomers are broadened beyond the detection limit and do not give rise to any observable signal. The spectra are characteristic of an unfolded peptide and unaltered over time, except for a uniform loss of intensity across the entire spectrum (Fig. 1, *Inset*). Therefore any significant population (>1% of total mass) of small oligomers detectable by NMR can be ruled out, in line with earlier findings for Aβ42 and islet amyloid polypeptide (8, 36). In the following, we thus interpret the time-dependent loss of the observed signals as reporting on the depletion of free monomers from the solution (36).

The NMR data show that the apparent lag phase for aggregation is shorter the lower the pH, in line with other studies (18, 37) (Fig. 1*A*). At all conditions, the experiments were repeated two or three times. Although there is some spread between repeats with regards to the length of the lag phase, the curve shape is pH dependent in a highly reproducible manner and all repeats fit well in the overall trend (Fig. 1*A* and *SI Appendix*, Fig. S1). In the pH range 7.1 to 8.6, each curve displays a single sigmoidal-like transition, which mirrors the type of curves obtained for ThT-monitored fibril formation as a function of time. Intriguingly, at pH 6.8 and below, we observe reproducible double-sigmoidal curves (Fig. 1*A* and *SI Appendix*, Fig. S1). At pH 6.8 the double-sigmoidal curve starts with a lag phase, followed by a first transition with a steep slope, which consumes ∼70% of the monomer. Between the two transitions, the free monomer concentration drops only slightly from 30 to around 20% of the starting intensity, at a much lower rate than during the transitions. The following second transition consumes most of the remaining monomer but the slope is less steep than that of the first transition. At lower pH (6.5 and 6.2) the first transition is completed faster and consumes more monomer (80% and 90%, respectively) and the intermediate plateau and second transition become less separated in time, compared to what is observed at pH 6.8. Importantly, the existence of an intermediate plateau at pH 6.2 to 6.8 indicates that monomer consumption is temporarily retarded, something which cannot be explained if the monomer consumption is the result of only nucleation and growth events. Additional processes must be considered in order to account for this peculiar kinetic profile.

ThT Fluorescence and Light Scattering. We also studied the aggregation reaction at pH 6.8 by ThT fluorescence and static light scattering. While NMR tracks the consumption of monomer, ThT fluorescence gives, under optimized conditions, a signal that is linearly proportional to the mass of ordered amyloid fibrils (8) and light scattering reports on the presence of aggregated species in general. In order to closely reproduce the conditions of the NMR experiment, the reaction was performed in the same type of NMR quartz tubes without stirring. The recorded signal, from ThT fluorescence and light scattering alike, increases for ∼7 h, and then decreases rapidly, so that after ∼9 h, ∼70% of the maximum intensity has been lost (Fig. 1 *B–D*). The time point at which this drop in intensity occurs closely coincides with the first decrease in reaction rate, i.e., the start of the intermediate plateau, monitored by NMR spectroscopy (*SI Appendix*, Fig. S2). The sudden decrease in ThT fluorescence can be explained by fibril sedimentation out of the excitation volume. Since the light path runs horizontally through a segment of the vertically oriented NMR tube, the recorded ThT signal is dependent on both the build-up of fibrils (increase in signal) and the fibril sedimentation out of the excitation volume (decrease in signal). Using time-lapse video (*SI Appendix*, Fig. S6, and Movie S1) recordings and sample homogenization (*SI Appendix*, Fig. S3) we confirmed that sedimentation is a contributing factor (full discussion to be found in *SI Appendix, Fig. S4*).

Cryo-Electron Microscopy. We used cryo-EM to investigate and compare the aggregates formed at different reaction time points at pH 6.8. Samples were withdrawn during the early reaction (2 h), close to the reaction midpoint (5 h, 9 h, and 10 h) and after the reaction end point (30 to 40 h). Each sample was taken from a separate reaction. The resulting cryo-EM images of samples taken during the early reaction reveal fibrils that are highly decorated with numerous filamentous protrusions extending from the sides of the fibrils (Fig. 2). These protrusions are thinner and appear to be more flexible than mature fibrils. At the earliest time point (2 h) there are examples of fibrils that are either completely free of covering protrusions or have protrusions that are very sparse and short. Toward the reaction midpoint it seems that the protrusions have grown longer (*SI Appendix*, Figs. S7 and S9). At the end of the reaction the surface decorations are almost completely absent and the samples are dominated by clear fibrils (Fig. 3 and *SI Appendix*, Figs. S8 and S9). Manual counting of clear and covered fibrils confirmed this trend in all samples tested (Fig. 4).

The reaction was repeated in the presence of the molecular chaperone domain prosurfactant protein C Brichos, which is found to suppress secondary nucleation (9). Samples were

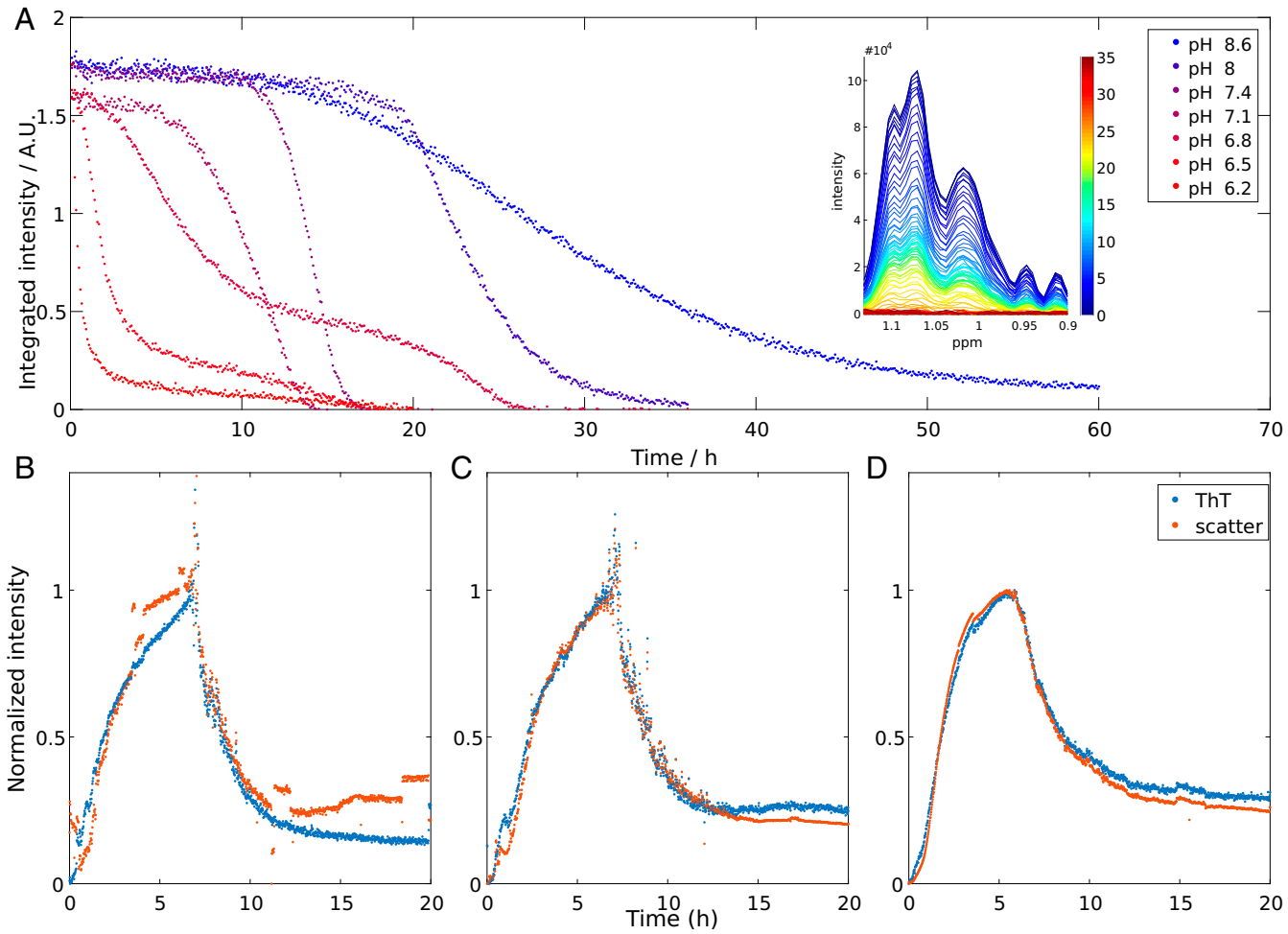

Fig. 1. (*A*) Aβ42 monomer concentration over time as monitored by the NMR signal intensity of methyl protons for reactions starting from 13.7 μM Aβ42 monomer at 37 °C at different pH values in 20 mM sodium phosphate buffer with 200 μM EDTA, 0.02% NaN_3, and 10% (vol/vol) D_2O. Representative data are shown, and repeats of the same conditions are shown in *SI Appendix*, Fig. S1. A.U. = arbitrary units. (*B–D*) ThT fluorescence intensity and light scattering from three independent experiments at 37 °C starting from 13.7 μM Aβ42 monomer at pH 6.8. Signals have been normalized to the approximate plateau values around 6 to 8 h.

withdrawn after 20 h, corresponding roughly to the reaction midpoint in this case. The resulting images (Fig. 5 and *SI Appendix*, Fig. S10) show a sample comprised of long fibrils, and separate from these fibrils are observed shorter, curlier filaments. There is only a low degree of association between the two; significant stretches of the fibrils are uncovered and large numbers of the filaments can be observed free in solution or associated to the carbon surfaces of the cryo-EM grid.

Seeded experiments were performed to investigate the aggregates formed after incubation of samples with controlled concentrations of monomers and fibrils present at the start of the reaction. Aβ42 fibrils (10% in monomer equivalents) were added to Aβ42 monomer solutions at pH 6.8 and incubated for 2 h before being withdrawn for imaging (Fig. 6*A* and *SI Appendix*, Fig. S11), yielding fibrils covered in protrusions that appear to be somewhat shorter and sparser than those in the unseeded samples, which can be related to the larger surface area to monomer concentration ratio in the seeded sample. At the end stage, in samples taken after 4 d, the fibrils are indistinguishable from those in the unseeded samples (*SI Appendix*, Fig. S11*D*).

For comparison, cross-seeding experiments were performed to investigate the specificity of protrusion formation. Aβ40 fibrils were added to Aβ42 monomer solutions at pH 6.8 and incubated for 2 h before being withdrawn for imaging (Fig. 6*C* and *SI Appendix*, Fig. S12). These samples contain a large number of fibrils completely devoid of surface coverage. In addition, there are several fibrils that are covered, much in the same way as in the unseeded samples and in the samples seeded with Aβ42 fibrils. In orthogonal experiments, samples containing Aβ40 monomer were supplemented at time 0 with Aβ42 fibrils (Fig. 6*B* and *SI Appendix*, Fig. S13); in these samples we observe well dispersed fibrils, highly ordered, with a well-defined twist and totally devoid of protrusions at the fibril surface.

In order to elucidate the potential role of the unstructured N terminus in this process we also prepared fibril samples where the endoprotease GluC was used to cut the Aβ peptide between Glu11 and V12. The fibrils prepared this way were added to Aβ42 monomer solutions in experiments analogous to the ones above, and incubated for 10 min before being withdrawn for imaging. Based on the images, it does not seem like any protrusions have formed on the surface of the treated fibrils (*SI Appendix*, Fig. S14).

Cross-Seeding Kinetics. Secondary nucleation and elongation show a high degree of specificity between Aβ40 and Aβ42; previous studies have shown that fibrils of neither species will accelerate the aggregation of the other one at physiological pH (26). In

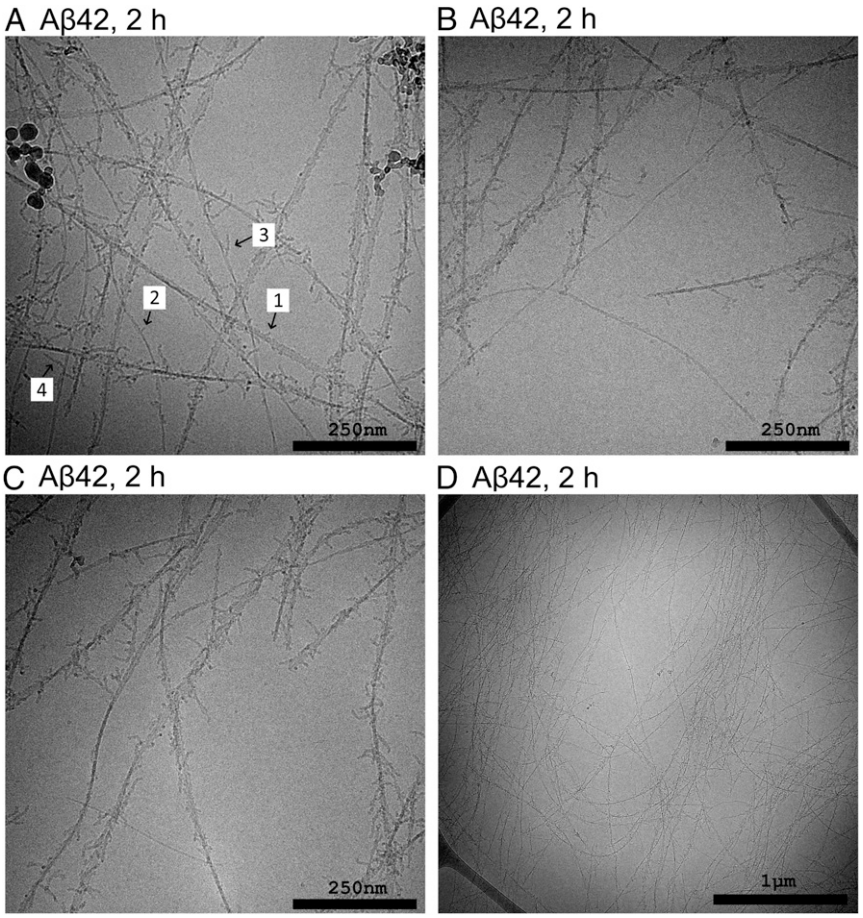

Fig. 2. Cryo-EM images of samples withdrawn after 2 h from the reaction starting from 13.7 μM Aβ42 monomer at pH 6.8. Almost all fibrils visible in this sample are covered by protrusions of varying lengths. (*A*) Close-up view where arrows indicate a few examples of different lengths numbered roughly in order of increasing length. (*B* and *C*) Close-up views showcasing that a few fibrils appear to be free of these protrusions or to be covered by significantly sparser and shorter protrusions. (*D*) Overview image.

order to extend those findings to the conditions of the present study a new set of cross-seeding kinetic experiments were performed at pH 6.8 (*SI Appendix*, Fig. S15). The kinetic profiles are very similar to those found at pH 7.4 (26): self-seeding increases the aggregation rate in a concentration-dependent manner while cross-seeding has a much smaller effect with a more complex influence. Fibrils of Aβ42 seem to have a slightly retarding effect on the aggregation of Aβ40. Conversely, fibrils of Aβ40 slightly accelerate the aggregation of Aβ42, but only at high seed concentration where elongation of the seeds may dominate.

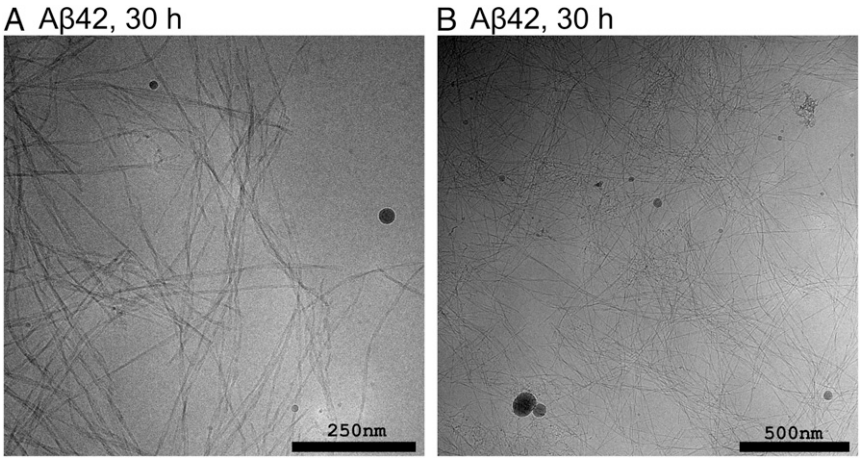

Fig. 3. Cryo-EM images of samples withdrawn after 30 h from the reaction starting from 13.7 μM Aβ42 monomer at pH 6.8. (*A*) Close-up view. (*B*) Overview. The samples are dominated by mature fibrils, not covered by any protrusions, with some clusters of unstructured material interspersed.

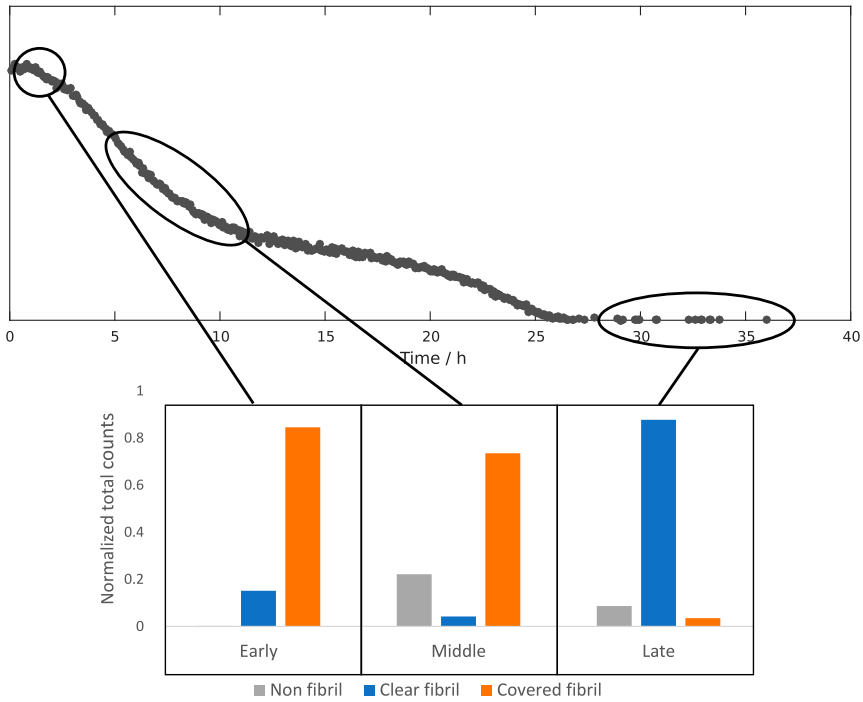

Fig. 4. A summary of the relative occurrence of different reaction species in all nonredundant images from the beginning (2 h, n = 3,172 counts from 32 images), middle (5 to 10 h n = 5,637 counts from 69 images), and end (30+ h n = 9,313 counts from 65 images) of the reaction. Fibrils covered by protrusions are very prevalent in the early to middle stages of the reaction and almost completely absent in the end.

Discussion

The double transition observed for Aβ42 aggregation at pH 6.8 was an unexpected finding which prompted further ultrastructural investigation using cryo-EM. The discovery of the heavily decorated fibrils at the reaction midpoint was equally surprising, and in order to learn more about their nature and their possible connection to the process of secondary nucleation, we performed additional experiments involving self- or cross-seeding or the presence of the chaperone Brichos.

Origin of Aggregation Intermediates. The cryo-EM images clearly show that nonfibrillar aggregates can transiently accumulate during the reaction. The emergence of decorated fibril intermediates is a highly reproducible finding seen in four separate experiments (Fig. 2 and *SI Appendix*, Figs. S7 and S9). The protrusions are qualitatively different from the parent fibrils in that they lack the characteristic stiffness, high level of structural ordering and a well-defined twist. The protrusions appear as strings of a repeated globular unit of ∼5 to 10 nm diameter. In this, they are similar in morphology to the prefibrillar structures termed protofibrils, which have been observed in early aggregation of Aβ42 (38, 39). Protofibrils are typically described as being composed of chains of globular oligomers with a high β-sheet content (40) and have been linked to cytotoxicity (41–43). Like the protrusions observed here, protofibrils tend to disappear toward the end of the reaction. Protofibrils are often isolated early in the aggregation (39, 44) or

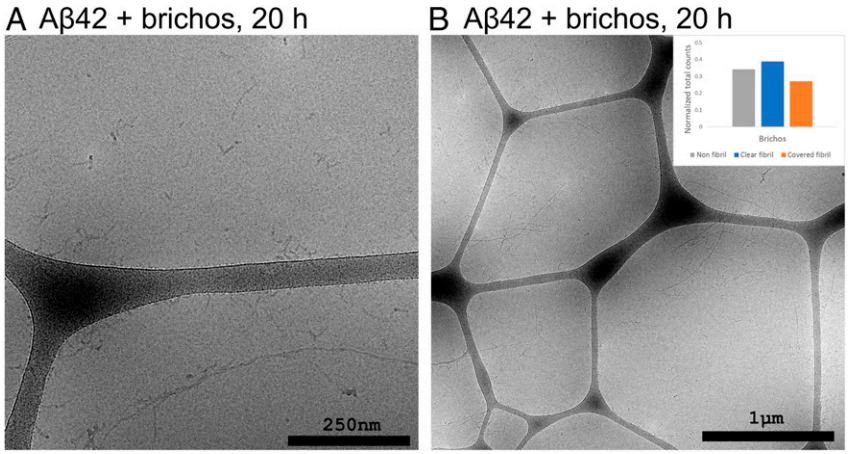

Fig. 5. Cryo-EM images of samples withdrawn after 20 h from the reaction starting from 13.7 μM Aβ42 monomer and 13.7 μM Brichos at pH 6.8. (*A*) Close-up view. (*B*) Overview. The fibrils are covered to a much lesser degree and there is a large number of free floating nonfibrillar structures. The *Inset* shows a summary of the relative occurrence of the different reaction species in all nonredundant images from this condition (n = 1,661 counts from 23 images).

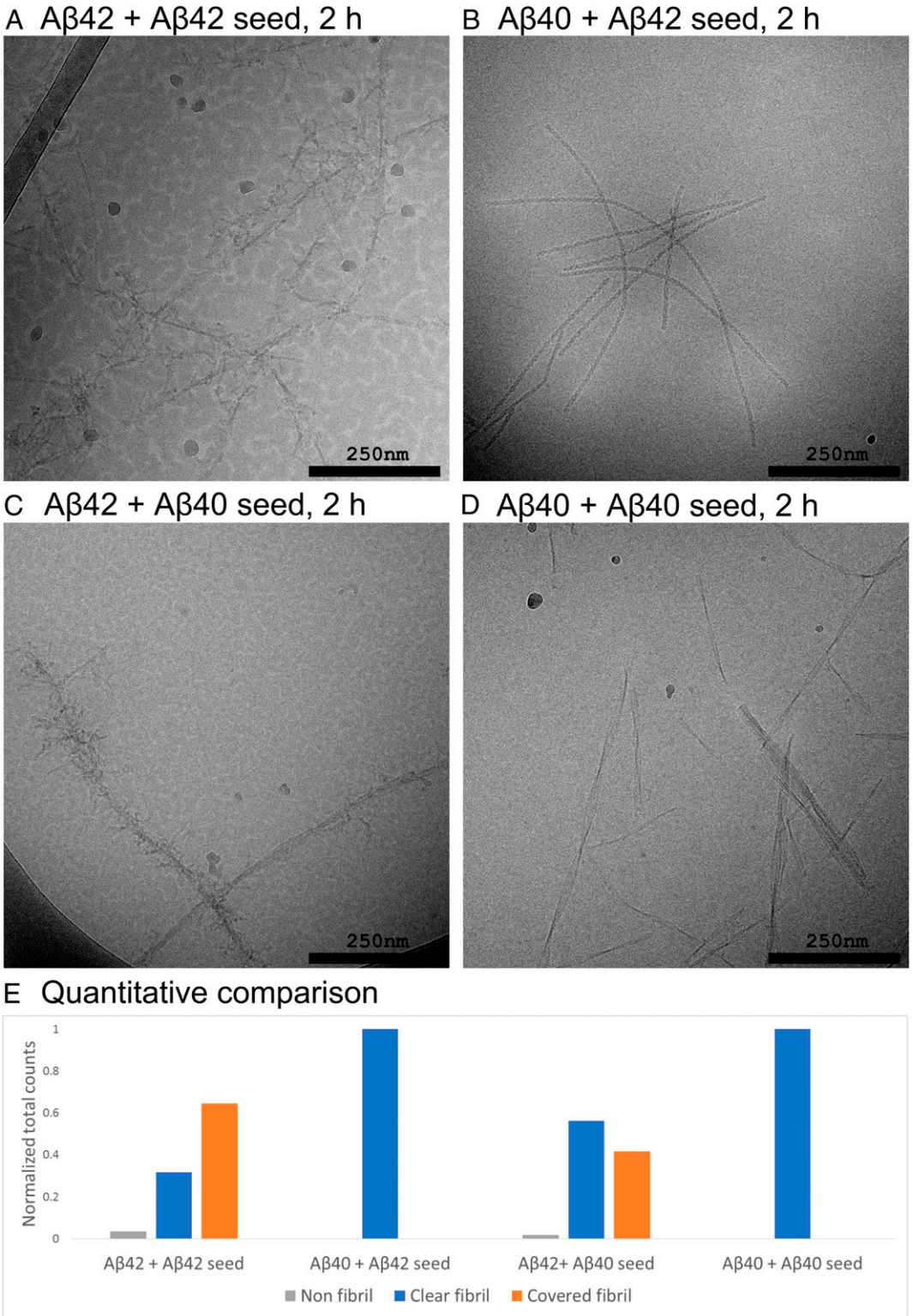

Fig. 6. Cryo-EM images of samples withdrawn from the reactions starting from 13.7 μM Aβ42 monomer at pH 6.8. (*A*) Supplemented with 1.4 μM (monomer equivalent concentration) of preformed fibrils of Aβ42. (*B*) From 13.7 μM Aβ40 monomer supplemented with 1.4 μM preformed fibrils of Aβ42. (*C*) From 13.7 μM Aβ42 monomer supplemented with 1.4 μM preformed fibrils of Aβ40. (*D*) From 13.7 μM Aβ40 monomer supplemented with 1.4 μM preformed fibrils of Aβ40. (*E*) Quantitative comparison of the relative abundance of the different reaction species in all nonredundant images from the different conditions (n = 798 counts from 11 images, n = 692 counts from 9 images, n = 1,860 counts from 12 images, and n = 2,593 counts from 22 images, respectively).

under conditions where formation of amyloid fibrils is suppressed by covalent modifications (45). It is thus relevant to ask whether the protrusions we see here can form in solution or if the fibril surface is necessary for initiation of their growth. Here, the intermediates are almost exclusively observed along the fibril surfaces. This implies that either the protrusions form on the fibril surface or that

they initially form in solution and are rapidly sequestered, which would require a very high diffusion rate and a high affinity for the fibril surface. In most cases where separate fibrils can be resolved, the protrusions seem to be attached with one end at the fibril surface, irrespective of their length (Fig. 2*A*), which also favors the interpretation that growth is initiated there. The large number of free floating protofibrils observed in the presence of Brichos (Fig. 5 and *SI Appendix*, Fig. S10) may support formation of protofibrils also in solution. It is likely that formation occurs both in solution and at the fibril surface, but at different rates, so that in the absence of inhibitor the surface catalyzed process dominates. Once a protofibril has been initiated, further growth is likely independent of whether it is attached to a fibril or not.

Location of Catalytic Sites. While previous work has shown the ability of antibody fragments (23) and chaperones (46) to selectively inhibit either secondary nucleation or elongation, implying that the sites for secondary nucleation are distinct from the sites for elongation (ends), we here provide ultrastructural evidence for accumulation of intermediates at the sides of fibrils along their entire length. In the images taken at the early to middle stages (2 to 10 h) of the unseeded reaction (Fig. 2 and *SI Appendix*, Figs. S7–S9) the majority of fibrils are covered in protrusions at a density that prevents any conclusions about the structural details. However, it is clear that the attachment occurs along the sides of fibrils and over their entire length. The influence of Brichos to drastically reduce the degree of surface coverage (Fig. 5 and *SI Appendix*, Fig. S10) provides indirect support that this attachment is relevant for secondary nucleation. A known inhibitor of secondary nucleation, Brichos has been shown by immunogold-EM to bind along the fibril surface (47) where it likely acts as competitive inhibitor (9).

Specificity of Surface Catalysis. Secondary nucleation by definition involves the nucleation of oligomers on the surface of aggregates composed of the same kind of monomers. However, the specificity of the surface nucleation process can be addressed using cross-seeding experiments with fibrils formed of sequence variants. Seeding of full-length monomers with fibrils composed of N-terminally truncated monomers, can address whether the unordered parts of the fibrils are equally important as the ordered core in the secondary nucleation process (21). The low amount of protrusions observed on the truncated fibrils (*SI Appendix*, Fig. S14) suggests that relatively unordered N-termini that decorate the fibrils of full-length monomers play a role in secondary nucleation.

A high specificity of surface nucleation is displayed in the case of the C-terminal length variants Aβ40 and Aβ42; monomers of each variant fail to nucleate on fibrils of the other one both at pH 7.4 (26) and at pH 6.8 (*SI Appendix*, Fig. S15). When supplementing a solution of Aβ42 monomers with premade Aβ40 fibrils (Fig. 5*C* and *SI Appendix*, Fig. S13) we observe two populations of fibrils after 2 h, one without any signs of protrusions, which is likely to be the premade Aβ40 fibrils, and one with protrusions which might be de novo formed Aβ42 fibrils. In the reverse experiment, where premade Aβ42 fibrils are added to a solution of Aβ40 monomers (Fig. 6*B* and *SI Appendix*, Fig. S13), we observe only fibrils without protrusions. Thus the absence of cross-nucleation (26) is mirrored by an absence of protrusions along the fibrils' sides.

Multistep Secondary Nucleation. The appearance of the decorated fibrils can be understood on the basis of the previously described multistep nature of secondary nucleation (Fig. 7) first identified for Aβ40 (7), but lately also for Aβ42 under conditions where the electrostatic repulsion is reduced (18, 20, 25). The steps may include attachment of monomers to the fibril surface, formation of oligomers, growth of the oligomers, structural conversion into fibrillar structure and detachment from the fibril surface. The order of the steps is still not fully determined (21) and the relative rates may vary with solution conditions, which can result in the accumulation of different intermediate species. The high degree of decoration observed here suggests a scenario in which the growth rate of oligomers by far exceeds the rate of detachment/conversion. The images from the samples seeded with Aβ42 fibrils (Fig. 6*A* and *SI Appendix*, Fig. S11) serve as another, intermediate condition. The lower ratio of monomer to fibrils leads to a lower ratio of arrival to detachment rates, compared to early times in the nonseeded experiment (Fig. 2), which yields a sparser coverage.

The growth rate depends on the monomer concentration and the concentration of protrusion ends. The rate of arrival to the catalytic sites on the fibrils depends on the monomer concentration and the concentration of available catalytic sites on the fibrils. On the other hand, the rate of detachment of aggregates formed by secondary nucleation is likely to be independent of the monomer concentration. Therefore, conditions may exist under which the resulting rates, governed by rate constants and concentrations, are such that growth of the newly formed aggregates exceeds their rate of detachment from the fibril surface. As the monomer concentration decreases at the end of the reaction, it can be expected that the rate of arrival will decrease to a value less than the rate of detachment, which would explain why only mature fibrils free of protrusions are observed in the cryo-EM images at the end of the reaction (Fig. 3).

Our ability to catch the transient structures on the fibril surface and image them by cryo-EM thus results from the study design to follow monomer consumption at multiple pH values in the range 6.2 to 8.6 and a fortuitous combination of the rates of the underlying microscopic processes at pH 6.8. Contributing factors are the high monomer concentration (13.7 μM, chosen to obtain a strong enough signal in the NMR experiments) and the reduced electrostatic repulsion at pH 6.8. With a lower concentration of monomer, especially at the levels typically found in vivo, such high degree of coverage would not be expected because the arrival and detachment rates are likely to be more closely matched. However, it stands to reason that the same underlying mechanism, binding at the fibril surface followed by structural conversion, would still be active and play a crucial role in the overall reaction.

Structural Conversion and Detachment. Since the protrusions are absent at the end of the reaction they must either undergo structural conversion into a fibrillar form or dissolve back to monomers. Protofibrils are generally believed to undergo structural conversion into fibrils and there have been direct observations of this taking place (48). A recent quantitative study on oligomer dynamics showed that the rate of conversion is lower than the rate of dissociation. Any given oligomer is thus more likely to dissolve than to convert but oligomer formation is a prerequisite for fibril formation (49).

The Origin of the Double Sigmoid. The serendipitous finding that initially prompted this investigation was the double sigmoidal profile observed at pH 6.8, where an initially fast rate of monomer depletion is temporarily decreased close to the reaction midpoint and subsequently increases again. This behavior cannot be captured by manipulating the rate constants of the existing models of nucleation and growth processes and implies that some other factor is influencing the effective rates. The timing suggests that there is a link between the decrease in reaction rate and the accumulation of protrusions along the fibril sides, but the nature of this link has not been conclusively determined. A likely explanation, given the observation of profuse sedimentation (*SI Appendix*, Fig. S6 and Movie S1), is that the decorated fibrils are more prone to associate into even larger

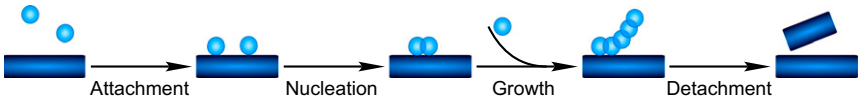

Fig. 7. Cartoon showing possible composite steps underlying secondary nucleation of monomers (spheres) on the surface of fibrils (rectangles). Monomers attach to the fibrils and undergo nucleation. As shown by the present study the aggregates can then grow by further monomer addition before they detach. Whether conversion into the mature fibrillar form happens before, during, or after detachment is still unclear.

aggregates, dramatically increasing the rate of sedimentation and thus depleting the solution of catalytic surfaces. Similar sedimentation was reported in 1906 to be observed during an ongoing crystallization process (11), and was recently observed during amyloid formation of Aβ40 at pH 7.5, 50 mM NaP, 100 mM NaCl (50). This scenario is supported by the reproduction of the observed double sigmoid by the addition of a fibril-depletion term (*SI Appendix*, Fig. S4). Another possibility is that the decorated fibrils form a network that is dense enough to hamper the diffusion of monomers, which would also temporarily reduce the reaction rate.

Conclusions

The current study presents clear evidence that secondary nucleation happens at the sides of fibrils and along the entire length of the fibrils, and that oligomeric species can grow into very large structures before they detach. Moreover, it seems that the attached species lack the high degree of order, with two filaments and a defined twist distances, seen in mature fibrils at the end of the reaction. The findings presented here prompt continued studies of secondary nucleation and serve as a basis for designing experiments to unravel its mechanistic and structural foundation.

Materials and Methods

Expression and Purification of Aβ(M1-42). Aβ(M1-42) was expressed in *Escherichia coli* (BL21 DE3 PLysS Star) from a PetSac vector carrying a synthetic gene with *E. coli*-preferred codons (51). The peptide was purified from inclusion bodies using sonication, ion exchange, and size exclusion steps as described (51). The amino acid sequence of the peptide is MDAEFRHDSGYEVHHQKLVFFAEDVGSNKGAIIGLMVGGVVIA.

Monomer isolation. Immediately prior to each experiment, Aβ42 was dissolved in 6 M guanidine hydrochloride, pH 8.0, and monomer was isolated by size exclusion chromatography (Superdex 75 column) in 20 mM sodium phosphate buffer with 200 μM ethylenediaminetetraacetic acid (EDTA), 0.02% NaN_3, pH 8.0. All purified samples were diluted to a concentration of 13.7 μM Aβ(M1-42) supplemented with 0 or 5 μM thioflavin T and the pH adjusted using sodium dihydrogen phosphate solution or disodium hydrogen phosphate solution.

Experimental conditions. The final samples contained 13.7 μM Aβ42 in 20 mM sodium phosphate at various pH values, 200 μM EDTA, 0.02% NaN_3, and 10% (vol/vol) D_2O. Samples for ThT fluorescence experiments further contained 5 μM ThT. All experiments were performed in NMR quartz tubes (500 μL sample volume) or quartz cuvettes (500 μL sample volume) at 37 °C under quiescent conditions.

NMR spectroscopy. Experiments were performed at 37 °C in NMR quartz tubes using an Agilent VNMRS DirectDrive spectrometer operating at a ^1H frequency of 600 MHz. The aggregation process was monitored via a series of one-dimensional ^1H spectra acquired over time periods of up to 60 h. Spectra were processed with NMRPipe (52). Methyl group signals were integrated in Matlab and the integrated values were plotted versus time. A heteronuclear single quantum coherence (HSQC) spectrum confirms close similarity with reported data (53).

Time lapse photography. Experiments were performed at 37 °C in NMR quartz tubes and pictures were taken every 10 min over time periods of up to 60 h.

ThT kinetics and static light scattering. The aggregation reaction was monitored in NMR quartz tubes or quartz cuvettes using a Probe Drum instrument (Probation Labs) by recording the ThT fluorescence (excitation 392 nm, emission 475 to 485 nm) at 1-min intervals over up to 60 h. The static light scattering signal was simultaneously obtained by recording the intensity of the excitation light (390 to 395 nm) at a 90° angle from the incident path.

Cryo-EM. For cryo-EM studies, experiments were performed using 13.7 μM Aβ42 in 20 mM sodium phosphate pH 6.8, 200 μM EDTA, 0.02% NaN_3, and 10% (vol/vol) D_2O, in four separate NMR tubes. For the first images, samples were withdrawn from two tubes after a 5-h incubation at 37 °C, the time point at which the reaction reached the first plateau. A second set of samples were taken from the remaining two tubes after 40 h when the reaction had reached the final plateau. This setup was repeated with an additional four tubes, using and older cryo-electron microscope and incubation times of 9 to 10 h and 30 to 33 h.

One sample with the same solution conditions supplemented with 13.7 μM Brichos was incubated for 20 h before being withdrawn for imaging.

For the seeding studies, four separate samples with the same solution conditions as above were prepared and two of them were supplemented with 1.4 μM premade Aβ42 fibrils and two with 1.4 μM premade Aβ40 fibrils. For each seed type one tube was incubated for 2 h and one for 4 d before being withdrawn for imaging. One sample was prepared with the same solution conditions, supplemented with 1.4 μM enzymatically truncated Aβ42 fibrils prepared according to the protocol below. This sample was incubated for 10 min before being withdrawn for imaging. The shorter incubation time was chosen to reduce the prevalence of de novo formed fibrils observed in the previous seeding experiments. In addition, one sample was prepared with 13.7 μM Aβ40 in the same solution conditions and supplemented with 1.4 μM premade Aβ42 fibrils.

A controlled environment vitrification system was used to ensure a stable temperature and to avoid the loss of solution during sample preparation. Samples were prepared as thin liquid films (<300 nm thick) on glow-discharge treated lacey carbon film coated copper grids and plunged into liquid ethane at −180 °C. In this way the original microstructures are preserved as component segmentation and rearrangement is avoided in addition to water crystallization as the samples are vitrified. Samples were stored under liquid N_2 until measured and then transferred using an Oxford CT3500 cryoholder and its workstation into the electron microscope (Philips CM120 BioTWIN Cryo) equipped with a postcolumn energy filter (Gatan GIF100). An acceleration voltage of 120 kV was used and images were recorded digitally with a charged-coupled device camera under low electron dose conditions.

Cross-seeding kinetics. The kinetic assay used 8 μM Aβ40 or 2 μM Aβ42 monomer in 20 mM sodium phosphate pH 6.8, 200 μM EDTA, 6 μM ThT, 0.02% NaN_3. The solution was supplemented with premade fibrils of Aβ40 and Aβ42 at concentrations of 1% and 10% of the initial monomer concentration. For comparison, a set of unseeded reactions were run in parallel. After mixing the monomer and the seeds the solutions were immediately incubated in a 96-well half-area plate of black polystyrene with a clear bottom and polyethylene glycol coating (Corning 3881) at 37 °C. The fluorescence was recorded in a Fluostar Omega plate reader (BMG Labtech) using a 440-nm excitation filter and a 480-nm emission filter.

Enzymatic N-terminal truncation. A solution of 10 μM Aβ42 monomer was supplemented with 1 μM premade Aβ42 fibrils and 0.1 μM endoprotease GluC and incubated at 37 °C. The fibrils prepared this way were used as the 1 μM seeds for a second round of fibrillation/digestion in the same conditions. The digestion process was confirmed by mass spectrometry showing a predominance of the 1010.43 Da Aβ(4-11) peptide in solution after digestion and fibril formation (*SI Appendix*, Fig. S16). The absence of the other peptides is likely due to AβM(1-3) being too small to be detected and Aβ(12-42) forming fibrils.

Quantification of images. Nonoverlapping images of sufficient quality were selected from each image set. The images were overlaid with a 16 × 16 grid. For each image the number of grid positions containing clear fibrils, fibrils decorated with protrusions, or nonfibrillar aggregates not attached to fibrils was counted. The number of counts was divided by the total number of counts in each set.

Data Availability. The kinetic data underlying Fig. 1 and *SI Appendix*, Figs. S1–S3, as well as the data underlying the image quantification graphs in Figs. 4 and 5, *Inset*, Fig. 6*E*, and *SI Appendix*, Fig. S14*E* can be found in Dataset S1. The data underlying the HSQC spectrum in *SI Appendix*, Fig. S5 and the full image sets from which the cryo-EM figures have been selected are available on Figshare (DOI: 10.0.23.196/m9.figshare.4715243).

ACKNOWLEDGMENTS. The expert help with cryo-EM by Anna Carnerup (Lund University) and the expert help with the mass spectrometry experiments by Katja Bernfur (Lund University) is gratefully acknowledged. This work was supported by grants from NanoLund (S.L.), Swedish Research Council (S.L. and M.A.), and the European Research Council (S.L.).

1. L. E. Hebert, J. Weuve, P. A. Scherr, D. A. Evans, Alzheimer disease in the United States (2010-2050) estimated using the 2010 census. *Neurology* **80**, 1778–1783 (2013).
2. J. Hardy, The amyloid hypothesis for Alzheimer's disease: A critical reappraisal. *J. Neurochem.* **110**, 1129–1134 (2009).
3. D. J. Selkoe, The therapeutics of Alzheimer's disease: Where we stand and where we are heading. *Ann. Neurol.* **74**, 328–336 (2013).
4. D. M. Walsh *et al*., Naturally secreted oligomers of amyloid β protein potently inhibit hippocampal long-term potentiation in vivo. *Nature* **416**, 535–539 (2002).
5. M. Lei *et al*., Soluble Aβ oligomers impair hippocampal LTP by disrupting glutamatergic/GABAergic balance. *Neurobiol. Dis.* **85**, 111–121 (2016).
6. A. Jan *et al*., Abeta42 neurotoxicity is mediated by ongoing nucleated polymerization process rather than by discrete Abeta42 species. *J. Biol. Chem.* **286**, 8585–8596 (2011).
7. G. Meisl *et al*., Differences in nucleation behavior underlie the contrasting aggregation kinetics of the Aβ40 and Aβ42 peptides. *Proc. Natl. Acad. Sci. U.S.A.* **111**, 9384–9389 (2014).
8. S. I. A. Cohen *et al*., Proliferation of amyloid-β42 aggregates occurs through a secondary nucleation mechanism. *Proc. Natl. Acad. Sci. U.S.A.* **110**, 9758–9763 (2013).
9. S. I. A. Cohen *et al*., A molecular chaperone breaks the catalytic cycle that generates toxic Aβ oligomers. *Nat. Struct. Mol. Biol.* **22**, 207–213 (2015).
10. H. E. C. Powers, Sucrose crystals. *Nature* **188**, 289–291 (1960).
11. H. A. Miers, F. Isaac, XLVII.—The refractive indices of crystallising solutions, with especial reference to the passage from the metastable to the labile condition. *J. Chem. Soc. Trans.* **89**, 413–454 (1906).
12. G. D. Botsaris, "Secondary nucleation—A review" in *Industrial Crystallization*, J. W. Mullin, Ed. (Springer, US, 1976), pp. 3–22.
13. F. A. Ferrone, J. Hofrichter, W. A. Eaton, Kinetics of sickle hemoglobin polymerization. II. A double nucleation mechanism. *J. Mol. Biol.* **183**, 611–631 (1985).
14. J. Anwar, S. Khan, L. Lindfors, Secondary crystal nucleation: Nuclei breeding factory uncovered. *Angew. Chem. Int. Ed. Engl.* **54**, 14681–14684 (2015).
15. A. Šarić *et al*., Physical determinants of the self-replication of protein fibrils. *Nat. Phys.* **12**, 874–880 (2016).
16. R. Frankel *et al*., Autocatalytic amplification of Alzheimer-associated Aβ42 peptide aggregation in human cerebrospinal fluid. *Commun. Biol.* **2**, 365 (2019).
17. A. K. Buell *et al*., Solution conditions determine the relative importance of nucleation and growth processes in α-synuclein aggregation. *Proc. Natl. Acad. Sci. U.S.A.* **111**, 7671–7676 (2014).
18. G. Meisl, X. Yang, B. Frohm, T. P. J. Knowles, S. Linse, Quantitative analysis of intrinsic and extrinsic factors in the aggregation mechanism of Alzheimer-associated Aβ-peptide. *Sci. Rep.* **6**, 18728 (2016).
19. A. Abelein, J. Jarvet, A. Barth, A. Gräslund, J. Danielsson, Ionic strength modulation of the free energy landscape of $A\beta_{40}$ peptide fibril formation. *J. Am. Chem. Soc.* **138**, 6893–6902 (2016).
20. X. Yang *et al*., On the role of sidechain size and charge in the aggregation of Aβ42 with familial mutations. *Proc. Natl. Acad. Sci. U.S.A.* **115**, E5849–E5858 (2018).
21. M. Törnquist *et al*., Secondary nucleation in amyloid formation. *Chem. Commun. (Camb.)* **54**, 8667–8684 (2018).
22. G. Meisl, X. Yang, C. M. Dobson, S. Linse, T. P. J. Knowles, A general reaction network unifies the aggregation behaviour of the Aβ42 peptide and its variants. arXiv: 160400828 Q-Bio (18 November 2016).
23. A. Munke *et al*., Phage display and kinetic selection of antibodies that specifically inhibit amyloid self-replication. *Proc. Natl. Acad. Sci. U.S.A.* **114**, 6444–6449 (2017).
24. F. A. Aprile *et al*., Selective targeting of primary and secondary nucleation pathways in Aβ42 aggregation using a rational antibody scanning method. *Sci. Adv.* **3**, e1700488 (2017).
25. G. Meisl, X. Yang, C. M. Dobson, S. Linse, T. P. J. Knowles, Modulation of electrostatic interactions to reveal a reaction network unifying the aggregation behaviour of the Aβ42 peptide and its variants. *Chem. Sci.* **8**, 4352–4362 (2017).
26. R. Cukalevski *et al*., The Aβ40 and Aβ42 peptides self-assemble into separate homomolecular fibrils in binary mixtures but cross-react during primary nucleation. *Chem. Sci.* **6**, 4215–4233 (2015).
27. M. Schmidt *et al*., Comparison of Alzheimer Abeta(1-40) and Abeta(1-42) amyloid fibrils reveals similar protofilament structures. *Proc. Natl. Acad. Sci. U.S.A.* **106**, 19813–19818 (2009).
28. M. Fändrich, M. Schmidt, N. Grigorieff, Recent progress in understanding Alzheimer's β-amyloid structures. *Trends Biochem. Sci.* **36**, 338–345 (2011).
29. C. Sachse, M. Fändrich, N. Grigorieff, Paired β-sheet structure of an Abeta(1-40) amyloid fibril revealed by electron microscopy. *Proc. Natl. Acad. Sci. U.S.A.* **105**, 7462–7466 (2008).
30. M. Schmidt *et al*., Peptide dimer structure in an Aβ(1-42) fibril visualized with cryo-EM. *Proc. Natl. Acad. Sci. U.S.A.* **112**, 11858–11863 (2015).
31. W. B. Stine Jr. *et al*., The nanometer-scale structure of amyloid-β visualized by atomic force microscopy. *J. Protein Chem.* **15**, 193–203 (1996).
32. J. S. Jeong, A. Ansaloni, R. Mezzenga, H. A. Lashuel, G. Dietler, Novel mechanistic insight into the molecular basis of amyloid polymorphism and secondary nucleation during amyloid formation. *J. Mol. Biol.* **425**, 1765–1781 (2013).
33. J. D. Harper, C. M. Lieber, P. T. Lansbury Jr., Atomic force microscopic imaging of seeded fibril formation and fibril branching by the Alzheimer's disease amyloid-β protein. *Chem. Biol.* **4**, 951–959 (1997).
34. M. T. Colvin *et al*., Atomic resolution structure of monomorphic $A\beta_{42}$ Amyloid fibrils. *J. Am. Chem. Soc.* **138**, 9663–9674 (2016).
35. M. A. Wälti *et al*., Atomic-resolution structure of a disease-relevant Aβ(1-42) amyloid fibril. *Proc. Natl. Acad. Sci. U.S.A.* **113**, E4976–E4984 (2016).
36. Y. Suzuki, J. R. Brender, K. Hartman, A. Ramamoorthy, E. N. G. Marsh, Alternative pathways of human islet amyloid polypeptide aggregation distinguished by (^{19})f nuclear magnetic resonance-detected kinetics of monomer consumption. *Biochemistry* **51**, 8154–8162 (2012).
37. A.-S. Johansson *et al*., Physiochemical characterization of the Alzheimer's disease-related peptides A β 1-42Arctic and A β 1-42wt. *FEBS J.* **273**, 2618–2630 (2006).
38. D. M. Walsh, A. Lomakin, G. B. Benedek, M. M. Condron, D. B. Teplow, Amyloid β-protein fibrillogenesis. Detection of a protofibrillar intermediate. *J. Biol. Chem.* **272**, 22364–22372 (1997).
39. J. D. Harper, S. S. Wong, C. M. Lieber, P. T. Lansbury Jr., Assembly of A β amyloid protofibrils: An in vitro model for a possible early event in Alzheimer's disease. *Biochemistry* **38**, 8972–8980 (1999).
40. C. Goldsbury, P. Frey, V. Olivieri, U. Aebi, S. A. Müller, Multiple assembly pathways underlie amyloid-beta fibril polymorphisms. *J. Mol. Biol.* **352**, 282–298 (2005).
41. B. Caughey, P. T. Lansbury, Protofibrils, pores, fibrils, and neurodegeneration: Separating the responsible protein aggregates from the innocent bystanders. *Annu. Rev. Neurosci.* **26**, 267–298 (2003).
42. D. M. Hartley *et al*., Protofibrillar intermediates of amyloid β-protein induce acute electrophysiological changes and progressive neurotoxicity in cortical neurons. *J. Neurosci.* **19**, 8876–8884 (1999).
43. H. A. Lashuel, D. Hartley, B. M. Petre, T. Walz, P. T. Lansbury Jr., Neurodegenerative disease: Amyloid pores from pathogenic mutations. *Nature* **418**, 291 (2002).
44. R. Kayed *et al*., Common structure of soluble amyloid oligomers implies common mechanism of pathogenesis. *Science* **300**, 486–489 (2003).
45. A. Sandberg *et al*., Stabilization of neurotoxic Alzheimer amyloid-beta oligomers by protein engineering. *Proc. Natl. Acad. Sci. U.S.A.* **107**, 15595–15600 (2010).
46. T. Scheidt *et al*., Secondary nucleation and elongation occur at different sites on Alzheimer's amyloid-β aggregates. *Sci. Adv.* **5**, eaau3112 (2019).
47. H. Willander *et al*., BRICHOS domains efficiently delay fibrillation of amyloid β-peptide. *J. Biol. Chem.* **287**, 31608–31617 (2012).
48. T. Watanabe-Nakayama *et al*., High-speed atomic force microscopy reveals structural dynamics of amyloid β1-42 aggregates. *Proc. Natl. Acad. Sci. U.S.A.* **113**, 5835–5840 (2016).
49. T. C. T. Michaels *et al*., Dynamics of oligomer populations formed during the aggregation of Alzheimer's Aβ42 peptide. *Nat. Chem.* **12**, 445–451 (2020).
50. A. Morinaga *et al*., Critical role of interfaces and agitation on the nucleation of Aβ amyloid fibrils at low concentrations of Aβ monomers. *Biochim. Biophys. Acta* **1804**, 986–995 (2010).
51. D. M. Walsh *et al*., A facile method for expression and purification of the Alzheimer's disease-associated amyloid β-peptide. *FEBS J.* **276**, 1266–1281 (2009).
52. F. Delaglio *et al*., NMRPipe: A multidimensional spectral processing system based on UNIX pipes. *J. Biomol. NMR* **6**, 277–293 (1995).
53. J. Roche, Y. Shen, J. H. Lee, J. Ying, A. Bax, Monomeric Aβ1–40 and Aβ1–42 peptides in solution adopt very similar Ramachandran map distributions that closely resemble random coil. *Biochemistry* **55**, 762–775 (2016).